Interplay between effective mass anisotropy and Pauli paramagnetic effects in a multiband superconductor: Application to Sr_2RuO_4

Noriyuki Nakai[1] and Kazushige Machida[1,2,*]

[1]*Department of Physics, Okayama University, Okayama 700-8530, Japan*

[2]*Department of Physics, Ritsumeikan University, Kusatsu 525-8577, Japan*

(Received 7 June 2015; revised manuscript received 23 July 2015; published 11 August 2015)

We investigate the mixed state properties in a type II multiband superconductor with uniaxial anisotropy under the Pauli paramagnetic effects. Eilenberger theory extended to a multiband superconductor is utilized to describe the detailed vortex lattice properties, such as the flux line form factors, the vortex lattice anisotropy, and magnetic torques. We apply this theory to Sr_2RuO_4 to analyze those physical quantities obtained experimentally, focusing on the interplay between the strong two-dimensional anisotropy and the Pauli paramagnetic effects. This study allows us to understand the origin of the disparity between the vortex lattice anisotropy ($\sim$60) and the H_{c2} anisotropy ($\sim$20). Among the three bands—γ with the effective mass anisotropy $\sim$180, α with $\sim$120, and β with $\sim$60—the last one is found to be the major band, responsible for various magnetic responses while the minor γ band plays an important role in the vortex formation. Namely, in a field orientation slightly tilted away from the two-dimensional basal plane those two bands cooperatively form the optimal vortex anisotropy which exceeds that given by the effective mass formula with infinite anisotropy. This is observed by small-angle neutron scattering experiments on Sr_2RuO_4. The pairing symmetry of Sr_2RuO_4 realized is either spin singlet or spin triplet with the d-vector strongly locked in the basal plane. The gap structure is that the major β band has a full gap and the minor γ band has a $d_{x^2-y^2}$-like gap.

DOI: 10.1103/PhysRevB.92.054505 PACS number(s): 74.25.Uv, 74.70.Pq, 74.25.Ha, 61.05.fg

I. INTRODUCTION

It is now widely recognized that multiband superconductors are omnipresent [1]. This recognition may be triggered by MgB_2 [2], where there exist two distinctive bands: the 3D π band and 2D-like σ band [3]. They play different roles in forming superconductivity, in particular in magnetic properties under an applied field, such as symmetry of vortex lattices [4] or the form factors probed by small-angle neutron scattering (SANS) experiments [5]. To understand its detailed magnetic response, a two-band model is indispensable. In fact different dimensionality of the band structures between the π band and σ band gives rise to rotation of the triangular vortex lattice under varying field [4]. The form factors of SANS experiments clearly demonstrate a gradual change of the two components of the π band and σ band as the field varies [5]. It is also true for other materials among unconventional and conventional superconductors where multiband description is essential, such as heavy-fermion superconductors [6,7] and iron pnictides [8,9].

We have been seeing that the Pauli paramagnetic effect (PPE) is important when combined with this multiband effect in certain superconductors, which give rise to a variety of unexpected phenomena. Typical examples are the oldest heavy-fermion superconductors $CeCu_2Si_2$ [6] and UBe_{13} [7] and also KFe_2As_2 [8,9], which necessitate the multiband description in fully understanding of their vortex properties. Those include the hidden first-order transition phenomenon [10] and the disparity [9] between the vortex lattice anisotropy and Fermi velocity anisotropy as discussed later.

Here we study the interplay between PPE and multiband effects in a uniaxial anisotropic superconductor in which each band has a different uniaxial anisotropy: For the case of two bands which we consider in this paper we can envisage two possible situations as schematically illustrated in Fig. 1. Let us consider the first case shown in Figs. 1(a) and 1(b). In the absence of PPE the two orbital-limited upper critical fields $H^{\rm orb}_{c2,\gamma}$ and $H^{\rm orb}_{c2,\beta}$ cross at A in the H versus Ω plane (Ω is the angle from the ab plane), each of which is characterized by the effective mass anisotropy Γ_i for two bands $i = \gamma$ and β, assuming $\Gamma_\gamma > \Gamma_\beta$. As indicated in Fig. 1(a) the four divided regions are characterized by each Γ_i. In particular, along $H_{c2}(\Omega)$ the characteristic anisotropy of the total system is switched at the intersecting point A from Γ_γ to Γ_β as Ω increases. When traversing at a higher H, the anisotropy Γ_γ for the γ band is sensed only.

Now let us switch on PPE; then both orbital-limited $H^{\rm orb}_{c2}(\Omega)$ are suppressed towards lower fields, especially Γ_γ if we assume that the superconducting gaps for the two bands such that $\Delta_\beta > \Delta_\gamma$. This is because the Pauli-limited fields $H^\beta_p > H^\gamma_p$. The resulting phase diagram is shown in Fig. 1(b). As seen from it the crossing point A is removed and three regions are now occupied by Γ_β while the Γ_γ region is hidden deep inside at lower fields and finite Ω's. In particular, along $H_{c2}(\Omega)$ the Γ_β region persists all the way from $\Omega = 0^\circ$ to $\Omega = 90^\circ$. Thus the higher field scan is sensing only the Γ_β anisotropy while a lower field scan is sensing $\Gamma_\beta \to \Gamma_\gamma \to \Gamma_\beta$ as Ω increases. This nontrivial anisotropy evolution is caused by the interplay between the effective mass anisotropy Γ and PPE.

Other possible phase diagrams are depicted in Figs. 1(c) and 1(d) where $\Delta_\beta < \Delta_\gamma$ is assumed, keeping $\Gamma_\gamma > \Gamma_\beta$. The γ (β) band with Δ_γ (Δ_β) is now major (minor). In the absence of PPE shown in Fig. 1(c) the two orbital-limited $H^{\rm orb}_{c2}(\Omega)$ curves are not crossed; thus the higher (lower) field region is occupied by Γ_γ (Γ_β). In the presence of PPE those curves are both suppressed downwards. Thus the two regions (Γ_γ and Γ_β) are simply shifted downwards, keeping its phase diagram

*Corresponding author: machida@mp.okayama-u.ac.jp

 ©2015 American Physical Society

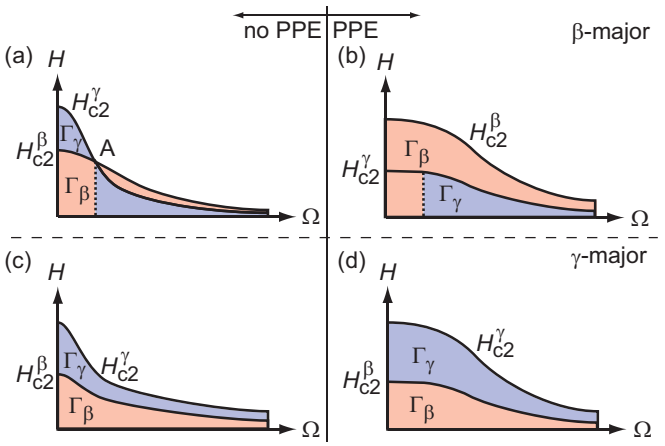

FIG. 1. (Color online) Schematic phase diagrams in the H versus Ω plane. The β band major scenario without PPE (a) and with PPE (b). The γ band major scenario without PPE (c) and with PPE (d). The effective mass anisotropy is assumed to be $\Gamma_\gamma > \Gamma_\beta$.

topologically unchanged. Note that $H_p^\beta < H_p^\gamma$. Therefore, a higher (lower) field scan is exclusively sensing the Γ_γ (Γ_β) anisotropy of the total system as Ω increases.

The purpose of this paper is to investigate the physics of Sr_2RuO_4 through the studies of the mixed state properties in this multiband superconductor where the interplay between the effective mass (or Fermi velocity) anisotropy and PPE is important in understanding of the vortex lattice state in H vs Ω plane. This superconductor is known to have strong two-dimensional uniaxial anisotropies for the three bands [11], the γ band ($\Gamma_\gamma \cong 180$), the α band ($\Gamma_\alpha \cong 120$), and the β band ($\Gamma_\beta \cong 60$). Given the density of states (DOS) N_{Fi} at the Fermi level ($N_{F\gamma} = 0.53$, $N_{F\alpha} = 0.10$, and $N_{F\beta} = 0.37$ of the total DOS), the α band is neglected in this paper for simplicity. In the following we consider a two-band model: the γ band with $N_{F\gamma} = 0.53$ and the β band with $N_{F\beta} = 0.47$.

In Sr_2RuO_4 there are several outstanding unsolved issues:
(1) Which band is the major band for superconductivity, the γ band or the β band? $\Delta_\beta > \Delta_\gamma$ or $\Delta_\beta < \Delta_\gamma$?
(2) Can the PPE resolve the observed disparity between the vortex lattice anisotropy [12] 60 and the H_{c2} anisotropy [11] 20?

The first issue (1) has been extensively debated, in particular in connection with the pairing mechanism of this material to stabilize the chiral p-wave state [13–17]. We approach this issue from a different view point by analyzing the mixed state vortex states. The second issue (2) has been investigated by us [18,19] based on the single-band picture. In this paper we revisit it based on a more realistic two-band model, which is able to allow us to study issue (1).

We base our computations on the quasiclassical theory [20–22]. The original single-band theory is extended to various multiband cases, including MgB_2 [23,24] and iron pnictides [25–27]. The applicability of the quasiclassical theory [20–22] is given in general by the condition $k_F\xi \gg 1$ with k_F the Fermi wave number and ξ the coherence length under the assumption that the normal state properties are described by a Fermi liquid theory. For Sr_2RuO_4 the three bands α, β, and γ are $k_F = 0.304$, 0.622, and 0.753 ($Å^{-1}$), respectively. The in-plane and c axis coherence lengths ξ are 660 and 33 (Å), respectively [11]. Thus for any combinations $k_F\xi \gg 1$ is well satisfied. We also notice that the lattice constants $a = 3.862$ Å and $c = 12.722$ Å are short enough compared with those coherence lengths; thus Sr_2RuO_4 is a three-dimensional normal metal. Moreover, most physical quantities, including various transport coefficients and thermodynamic properties, can be consistently and coherently described by a Fermi liquid theory as explained in detail by Mackenzie and Maeno [11]. Therefore we can quite safely apply the quasiclassical theory to Sr_2RuO_4.

By self-consistently solving microscopic quasiclassical Eilenberger equation with two bands, we calculate a variety of the physical quantities relevant to available experiments, such as the form factors probed by SANS experiments [12,28], magnetic torques [29], and the vortex lattice anisotropy Γ_{VL}, which differs generally from the effective mass anisotropy Γ_i mentioned above.

The arrangement of this paper is as follows: After introducing Eilenberger theory extended to multibands [24] with PPE in Sec. II, which was done in our previous paper [10], we construct a model system for considering Sr_2RuO_4 by fixing the several model parameters in Sec. III. Here we compare the two scenarios—one is the β major and the other γ in equal footing—finding that the former is better than the latter relative to the existing experiments. Then we come to the main theme of the present paper in Sec. IV: computations and analyses of the form factors and vortex lattice anisotropies as a function of the angle Ω compared with the data of SANS experiments [9,12]. In Sec. V we examine the magnetic torques which are also measured recently by Kittaka *et al.* [29]. The final section, Sec. VI, is devoted to discussion and conclusion. This paper is an extension of our previous work based on a single-band model [19,30,31] and is also closely related to our two-band model calculations [10,24].

II. QUASICLASSICAL THEORY INCLUDING PPE FOR TWO BANDS

We start with the free energy F in the quasiclassical theory [20–22] extended to the two-band case [23–27], which is given by

$$F = \int d\boldsymbol{r}\left\{\frac{|B(\boldsymbol{r})|^2}{8\pi} - \frac{\chi_n}{2}|B(\boldsymbol{r})|^2 + \Sigma_{i,j}\Delta_j^*(\boldsymbol{r})(\hat{V}^{-1})_{i,j}\Delta_i(\boldsymbol{r}) - \pi k_B T N_{F0}\Sigma_{|\omega_n|<\omega_c}\Sigma_j \frac{N_{Fj}}{N_{F0}}\langle I(\omega_n,\boldsymbol{k}_j,\boldsymbol{r})\rangle_{\boldsymbol{k}_j}\right\} \quad (1)$$

with $\chi_n = 2\mu_B^2 N_{F0}$, $N_{F0} = \Sigma_j N_{Fj}$, and

$$I(\omega_n,\boldsymbol{k}_j,\boldsymbol{r}) = \Delta(\boldsymbol{k}_j,\boldsymbol{r})f^\dagger(\omega_n,\boldsymbol{k}_j,\boldsymbol{r}) + \Delta^*(\boldsymbol{k}_j,\boldsymbol{r})f(\omega_n,\boldsymbol{k}_j,\boldsymbol{r}) + [g_j - \mathrm{sgn}(\omega_n)]\left\{\frac{1}{f_j}\left[\omega_n + i\mu_B B + \frac{\hbar}{2}\boldsymbol{v}_{Fj}\cdot\left(\vec{\nabla} - i\frac{2\pi}{\phi_0}\boldsymbol{A}\right)\right]f_j + \frac{1}{f_j^\dagger}\left[\omega_n + i\mu_B B - \frac{\hbar}{2}\boldsymbol{v}_{Fj}\cdot\left(\vec{\nabla} + i\frac{2\pi}{\phi_0}\boldsymbol{A}\right)\right]f_j^\dagger\right\}. \quad (2)$$

The flux quantum $\phi_0 = \frac{hc}{2|e|}$. $\boldsymbol{v}_{\mathrm{F}j}$ is the Fermi velocity at $\boldsymbol{k}_j$ of the band j. The Fermi surface average $\langle\cdots\rangle_{\mathbf{k}_j}$ is normalized within each band as $\langle 1\rangle_{\mathbf{k}_j} = 1$. Here we introduced the interaction matrix V_{ij} with 2×2 for two bands, where V_{jj} is the pairing interaction on the j band and $V_{ij} = V_{ji}$ for $i \neq j$ is the Cooper pair transfer between the i and j bands. $g_j = g(\omega_n,\boldsymbol{k}_j,\boldsymbol{r})$, $f_j = f(\omega_n,\boldsymbol{k}_j,\boldsymbol{r})$, and $f_j^\dagger = f^\dagger(\omega_n,\boldsymbol{k}_j,\boldsymbol{r})$ are the quasiclassical Green's functions for the j band. $\Delta_j(\boldsymbol{k}_j,\boldsymbol{r}) = \Delta_j(\boldsymbol{r})\phi_j(\boldsymbol{k}_j)$ is the pair potential and $\phi_j(\boldsymbol{k}_j)$ describes the gap symmetry of the j band in reciprocal space, which allows us to choose the gap form depending on each band as will be done in the following. The vector potential $\boldsymbol{A}(\boldsymbol{r})$ and the internal field $\boldsymbol{B}(\boldsymbol{r})$ are related to $\boldsymbol{B}(\boldsymbol{r}) = \nabla\times\boldsymbol{A} = \bar{\boldsymbol{B}} + \boldsymbol{b}(\boldsymbol{r})$ with $\bar{\boldsymbol{B}}$ uniform field.

By following the same procedure by Eilenberger [20], the functional derivatives with respect to $f_j = f(\omega_n,\boldsymbol{k}_j,\boldsymbol{r})$ and $f_j^\dagger = f^\dagger(\omega_n,\boldsymbol{k}_j,\boldsymbol{r})$ yield the so-called Eilenberger equation extended to the two band case:

$$\begin{aligned}\{\omega_n + i\mu B(\boldsymbol{r}) + \boldsymbol{v}_{\mathrm{F}j}\cdot[\nabla + iA(\boldsymbol{r})]\}f_j &= \Delta_j(\boldsymbol{k}_j,\boldsymbol{r})g_j,\\ \{\omega_n + i\mu B(\boldsymbol{r}) - \boldsymbol{v}_{\mathrm{F}j}\cdot[\nabla - iA(\boldsymbol{r})]\}f_j^\dagger &= \Delta_j^*(\boldsymbol{k}_j,\boldsymbol{r})g_j.\end{aligned} \tag{3}$$

This form is understandable because the fourth term in the free energy Eq. (1), which includes the Green's functions, is separable in the band index; thus the resultant equation of the functional derivative should be separable for each band. The stationary conditions of Eq. (1) with respect to the functionals $\Delta_j^*(\boldsymbol{r})$ and the vector potential $\boldsymbol{A}(\boldsymbol{r})$ give rise to a complete set of the self-consistent equations extended to the two-band case, which are given below: Eqs. (4) and (5). This complete set of the self-consistent equations coincides and is consistent with those obtained previously [23,24].

The electronic state is calculated by solving the Eilenberger equation Eq. (3) in the clean limit [32], including the Pauli paramagnetic effect (PPE) due to the Zeeman term $\mu B(\boldsymbol{r})$ [33], where $\mu = \mu_{\mathrm{B}}B_0/\pi k_B T_{\mathrm{c}}$ is a renormalized Bohr magneton related to the so-called Maki parameter $\alpha_{\mathrm{M}} = 1.76\mu$. The quasiclassical Green's functions $g(\boldsymbol{k}_j,\boldsymbol{r},\omega_n + i\mu B)$, $f(\boldsymbol{k}_j,\boldsymbol{r},\omega_n + i\mu B)$, and $f^\dagger(\boldsymbol{k}_j,\boldsymbol{r},\omega_n + i\mu B)$ with the band index j depend on the direction of the Fermi momentum $\boldsymbol{k}_j$ for each band, the center-of-mass coordinate $\boldsymbol{r}$ for the Cooper pair, and Matsubara frequency $\omega_n = (2n+1)\pi k_{\mathrm{B}}T$ with $n\in\mathbb{Z}$. They are calculated in a unit cell of the triangle vortex lattice.

The unit of Fermi velocity $v_{\mathrm{F}0}$ is defined by $N_{\mathrm{F}0}v_{\mathrm{F}0}^2 \equiv N_{\mathrm{F}1}v_{\mathrm{F}1}^2 + N_{\mathrm{F}2}v_{\mathrm{F}2}^2$, where the density of states (DOS) in the normal state at each Fermi surface is defined by $N_{\mathrm{F}0} \equiv N_{\mathrm{F}1} + N_{\mathrm{F}2}$. Throughout this paper, temperatures, energies, lengths, and magnetic fields are, respectively, measured in units of the transition temperature T_{c}, $\pi k_{\mathrm{B}}T_{\mathrm{c}}$, $\xi_0 = \hbar v_{\mathrm{F}0}/2\pi k_{\mathrm{B}}T_{\mathrm{c}}$, and $B_0 = \phi_0/2\pi\xi_0^2$. We calculate the spatial structure of g in a fully self-consistent way.

The pairing potential $\Delta_j(\mathbf{r})$ is calculated by the gap equation

$$\Delta_j(\boldsymbol{r}) = T\sum_{0<\omega_n\leqslant\omega_{\mathrm{c}}}\sum_{l=1,2}V_{jl}N_{\mathrm{F}l}\langle(f_l + f_l^{\dagger *})\phi_l(\boldsymbol{k}_l)\rangle_{\boldsymbol{k}_l}, \tag{4}$$

which is coupled via the interaction matrix $\hat{V}$. We use the energy cutoff $\omega_{\mathrm{c}} = 20k_{\mathrm{B}}T_{\mathrm{c}}$. The vector potential is also self-consistently determined by

$$\nabla\times\nabla\times\boldsymbol{A} = \nabla\times\boldsymbol{M}_{\mathrm{para}} - \frac{T}{\kappa^2}\sum_{|\omega_n|\leqslant\omega_{\mathrm{c}}}\sum_{j=1,2}N_{\mathrm{F}j}\langle\boldsymbol{v}_j\mathrm{Im}[g_j]\rangle_{\boldsymbol{k}_j}, \tag{5}$$

which includes the contribution of the paramagnetic moment $\boldsymbol{M}_{\mathrm{para}} = (0,0,M_{\mathrm{para}})$ with

$$M_{\mathrm{para}} = M_0\left(\frac{B(\boldsymbol{r})}{\bar{B}} - \frac{T}{\mu\bar{B}}\sum_{|\omega_n|<\omega_{\mathrm{c}}}\sum_{j=1,2}N_{\mathrm{F}j}\langle\mathrm{Im}[g_j]\rangle_{\boldsymbol{k}_j}\right). \tag{6}$$

Here $\bar{B}$ is the averaged flux density mentioned above, the normal state paramagnetic moment $M_0 = (\mu/\kappa)^2\bar{B}$, and $\kappa = B_0/\pi k_{\mathrm{B}}T_{\mathrm{c}}\sqrt{8\pi N_{\mathrm{F}0}}$. The Ginzburg-Landau (GL) parameter κ_{GL} is the ratio of the penetration depth to coherence length for $\bar{\boldsymbol{B}} \parallel c$. Using Doria-Gubernatis-Rainer scaling [34], we obtain the relation [32] of $\bar{B}$ and the external field H. The total magnetization $M_{\mathrm{total}} = \bar{B} - H$ including both the diamagnetic and the paramagnetic contributions is derived.

We solve Eq. (3) with $i\omega_n \to E + i\eta$ for the electronic state. The local density of states (LDOS) is given by $N_j(\boldsymbol{r},E) = N_{j,\uparrow}(\boldsymbol{r},E) + N_{j,\downarrow}(\boldsymbol{r},E)$, where

$$N_{j,\sigma}(\boldsymbol{r},E) = N_{\mathrm{F}j}\langle\mathrm{Re}[g(\boldsymbol{k}_j,\boldsymbol{r},\omega_n + i\sigma\mu B)|_{i\omega_n\to E+i\eta}]\rangle_{\boldsymbol{k}_j}, \tag{7}$$

with $\sigma = 1$ (-1) for up (down) spin component. We typically use the smearing factor $\eta = 0.01$. The DOS is obtained by the spatial average of the LDOS as $N(E) = \sum_j N_j(E) = \sum_j\langle N_{j,\uparrow}(\boldsymbol{r},E) + N_{j,\downarrow}(\boldsymbol{r},E)\rangle_{\boldsymbol{r}}$.

We consider a simplified model of a two-band system with a larger superconducting gap band (band 1) and a smaller gap band (band 2). As a model of the Fermi surfaces, we use two quasi-two-dimensional Fermi surfaces with rippled cylinder shapes. The Fermi velocity is assumed to be $\mathbf{v}_j = (v_{j,a},v_{j,b},v_{j,c}) \propto (\cos\phi,\sin\phi,\tilde{v}_{j,z}\sin k_{j,c})$ at $\mathbf{k}_j = (k_{j,a},k_{j,b},k_{j,c}) \propto (k_j\cos\phi,k_j\sin\phi,v_{j,c})$ on the Fermi surfaces [35]. We consider a case $\tilde{v}_{j,z} = 1/\Gamma_j$, to produce large anisotropy ratio of the coherence lengths,

$$\Gamma_j = \xi_{j,c}/\xi_{j,b} \sim \left\langle v_{j,c}^2\right\rangle_{\mathbf{k}_j}^{1/2}\Big/\left\langle v_{j,b}^2\right\rangle_{\mathbf{k}_j}^{1/2} \tag{8}$$

with $j = 1,2$, where $\langle\cdots\rangle_{\mathbf{k}_j}$ indicates an average over the Fermi surface on each band. The magnetic field orientation is tilted by $\theta \equiv 90^\circ - \Omega$ from the c axis towards the ab plane. Since we set the z axis to the vortex line direction, the coordinate $\mathbf{r} = (x,y,z)$ for the vortex structure is related to the crystal coordinate (a,b,c) as $(x,y,z) = (a,b\cos\theta + c\sin\theta, c\cos\theta - b\sin\theta)$.

We set unit vectors of the vortex lattice as

$$\mathbf{u}_1 = c(\alpha/2,-\sqrt{3}/2), \quad \mathbf{u}_2 = c(\alpha/2,\sqrt{3}/2) \tag{9}$$

with $c^2 = 2\phi_0/(\sqrt{3}\alpha\bar{B})$ and the vortex lattice anisotropy is defined by $\Gamma_{\mathrm{VL}} = \alpha/\sqrt{3}$. The anisotropic ratio $\Gamma_j(\theta) \equiv \xi_{j,y}/\xi_{j,x} \sim \langle v_{j,y}^2\rangle_{\mathbf{k}_j}^{1/2}/\langle v_{j,x}^2\rangle_{\mathbf{k}_j}^{1/2}$, which comes from the Fermi

velocity anisotropy,

$$\Gamma_j(\theta) = \frac{1}{\sqrt{\cos^2\theta + \Gamma_j^{-2}\sin^2\theta}} \tag{10}$$

with $j = 1$ and 2.

To discuss $\bar{B}$ dependence of the internal field distribution $B(\mathbf{r}) = \nabla \times \boldsymbol{A}$, we consider flux line lattice (FLL) form factor $\boldsymbol{F}(\mathbf{q}_{h,k}) = (F_{x(h,k)}, F_{y(h,k)}, F_{z(h,k)})$, which is obtained by Fourier transformation of the internal field distribution as $\boldsymbol{B}(\mathbf{r}) = \sum_{h,k} \boldsymbol{F}(\mathbf{q}_{h,k}) \exp(i\mathbf{q}_{h,k}\cdot\mathbf{r})$ with the wave vector $\mathbf{q}_{h,k} = h\mathbf{q}_1 + k\mathbf{q}_2$. h and k are integers. The unit vectors in reciprocal space are given by $\mathbf{q}_1 = (2\pi/c)(1/\alpha, -1/\sqrt{3})$ and $\mathbf{q}_2 = (2\pi/c)(1/\alpha, 1/\sqrt{3})$. The z component $|F_{z(h,k)}|^2$ from $B_z(\mathbf{r})$ gives the intensity of conventional non-spin-flip SANS. The transverse component, $|F_{\mathrm{tr(h,k)}}|^2 = |F_{x(h,k)}|^2 + |F_{y(h,k)}|^2$, is accessible by spin-flip SANS experiments [12,36].

III. MODEL CONSTRUCTION AND PHYSICS FOR $H \parallel c$

A. Specific heat and H_{c2} anisotropy ratio

In order to determine the model parameters appropriate for Sr_2RuO_4, we start out to fix the gap magnitudes $\Delta_\gamma(T)$ and $\Delta_\beta(T)$ and their nodal structures. We first analyze the electronic specific heat data $C(T)/T$ at zero field [37] by solving self-consistently the Eilenberger equation Eq. (3) for the uniform system without using the phenomenological so-called α model [38]. Here we have assumed that the minor component is induced only by the Cooper pair transfer coupling V_{12}. The direct attractive coupling among the minor component is vanishing; $V_{22} = 0$.

As seen from Fig. 2 the $C(T)/T$ data are equally well explained either by

(A) the γ scenario with $\Delta_\gamma(0)/\Delta_\beta(0) = 1.7$ at $T = 0$ where both bands have line nodes, in agreement with other authors [14], or

(B) the β scenario with $\Delta_\beta(0)/\Delta_\gamma(0) = 2.5$ where the β band has a full gap and the γ band line nodes.

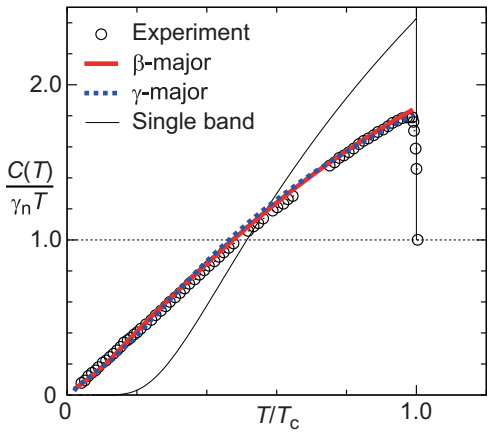

FIG. 2. (Color online) The specific heat data (open symbols) [37] analysis by the β-major scenario (bold line) with $\Delta_\beta(0)/\Delta_\gamma(0) = 2.5$ where the line node (full) gap is on the γ (β) band and by the γ-major scenario (dotted line) with $\Delta_\gamma(0)/\Delta_\beta(0) = 1.7$, where both bands contain the line nodes. For comparison, the standard BCS case with the full gap is also shown (thin line).

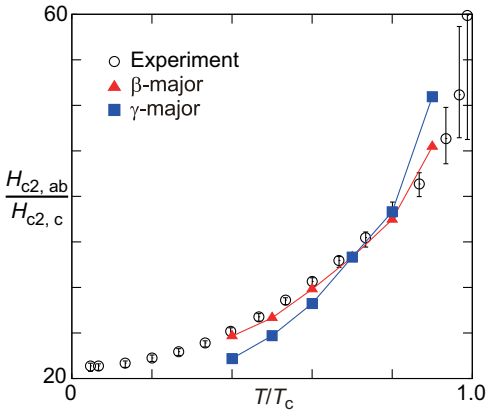

FIG. 3. (Color online) The upper critical field ratio $H_{c2,ab}(T)/H_{c2,c}(T)$ for the two directions ($H \parallel ab$ and $H \parallel c$). The two cases for the β (filled triangles) and γ scenarios (filled squares) are compared with the experimental data (open symbols) [39]. This shows that the β scenario is superior to the γ scenario.

It is apparent that the linear T behavior of $C(T)/T$ at lower T indicates that the nodal gap is necessary somewhere: for the γ scenario in both bands and for the β scenario only in the γ band. This nodal structure difference between them is decisive for the two scenarios as will be seen shortly.

According to Kittaka *et al.* [39], the upper critical field ratio $H_{c2,ab}(T)/H_{c2,c}(T)$ for the two directions ($H \parallel ab$ and $H \parallel c$) is T dependent, implying that PPE becomes stronger as the field applied to the ab plane increases. Here we calculate $H_{c2,ab}(T)/H_{c2,c}(T)$ for both scenarios and depict the results in Fig. 3. Since near T_c the intrinsic effective mass anisotropy governs its tending limit ($T \to T_c$), $H_{c2,ab}/H_{c2,c} \to 180$ (60) for the γ (β) scenario. The experimental data [39] shown support the β scenario within the experimental accuracy where there is no indication of the ratio with tending to 180. This is one of the most clear signatures for the β-major scenario. By adjusting the μ parameters for both scenarios the best fittings are accomplished in $\mu = 0.04$ (0.02) for the β (γ) scenario. From now on we use those values in the following calculations.

In order to further distinguish between the two scenarios, we take up the experimental data [37] of the field dependence of $C(H)/T$ for $H \parallel c$ at the available lowest temperature $T = 60$ mK, which best mimics the zero-energy density of states $N(H)$ at $T = 0$ in the theoretical calculation. In Fig. 4 we compare the experimental data with the theoretical values as a function of the field applied parallel to the c axis. As seen from it, the γ scenario overestimates the data while the β scenario underestimates it. If taking into account the finite-T effect in the experimental data, the theoretical curves should move up when considering thermal excitations, resulting in further departure of the γ-major curve while the β-major curve comes closer to the data. We also note from Fig. 4 that too many low-energy excitations are released at lower fields in the γ scenario because the nodal gap exists in the minor band, causing the overestimate. This fact, which has been unnoticed so far, is quite fatal for the γ scenario.

Thus it is clear from those two criteria that the β scenario is far better than the γ scenario. The best fitting also yields the κ_{GL} value for $H \parallel c$, that is, $\kappa_{\mathrm{GL}} = 2.7$, whose value is used in

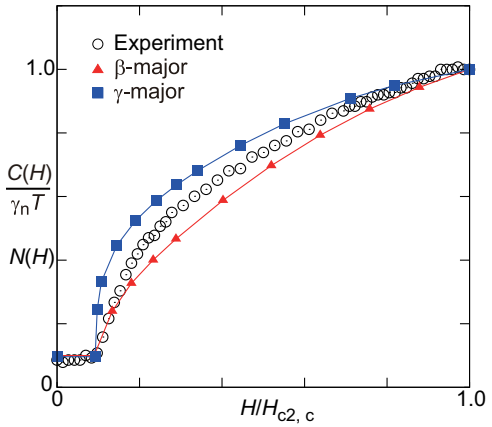

FIG. 4. (Color online) The comparison of the experimental data (open symbols) [37] of the specific heat at $T = 60$ mK as a function of $H(\| c)$ with the theoretical results (filled symbols) for the β and γ scenarios ($T = 0.1T_c$). This shows too many low-energy excitations released at lower fields in the γ scenario because the nodal gap exists in the minor band.

the following computations. But we should keep in mind that this low κ_{GL} value delicately depends on the particular sample used. This quantity is known to be sample dependent.

B. Form factors for $H \parallel c$

The form factors of the longitudinal components $F_{z(10)}$ and $F_{z(11)}$, which are measured by SANS experiments [40] for $H \parallel c$, are compared with the two scenarios whose magnitudes are multiplied by a factor of 1.7 for the β scenario and 3.5 for the γ scenario. This is partly because the actual $\kappa_{GL} = 2.7$ determined by $C(H)/T$ fitting previously might be different from the SANS experiment (in fact $H_{c2,c} = 58$ mT and $\kappa_{GL} = 2.0$ differ from $H_{c2,c} = 75$ mT and $\kappa_{GL} = 2.3$ in the best samples [11]). Since the form factor magnitudes are sensitive to the κ_{GL} value ($\propto \kappa_{GL}^{-2}$), it is permissible to adjust it to fit with data. As seen from Fig. 5 the field dependencies of $F_{z(10)}$ and $F_{z(11)}$ are far better explained by the β scenario than by the γ scenario.

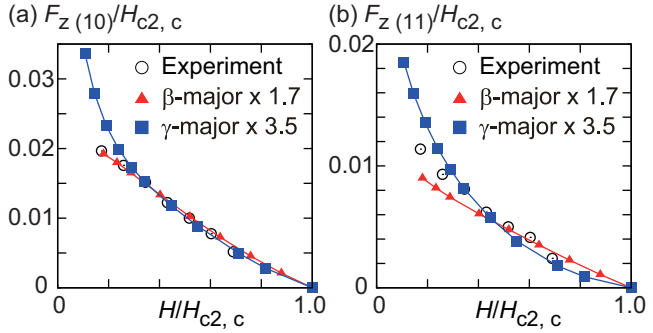

FIG. 5. (Color online) The longitudinal form factors $F_{z(10)}$ and $F_{z(11)}$ as a function of $H(\| c)$. The experimental data (open symbols) [40] are compared with the two scenarios. The theoretical results (filled symbols) are multiplied by a factor 1.7 (3.5) for the β (γ) case ($T = 0.1T_c$). This shows that the β scenario is superior to the γ scenario.

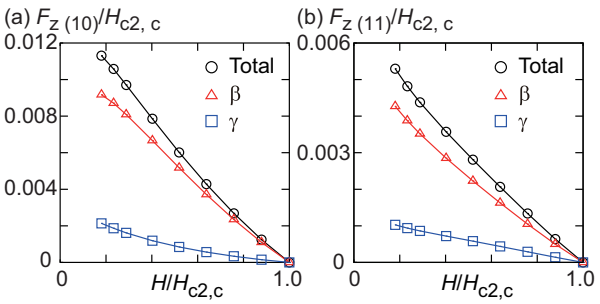

FIG. 6. (Color online) The longitudinal form factors $F_{z(10)}$ and $F_{z(11)}$ are decomposed into the the β band contribution and γ band contribution in the case of the β scenario ($T = 0.1T_c$).

In Fig. 6 we decompose the longitudinal form factors $F_{z(10)}$ and $F_{z(11)}$ into the two contributions of the β band and γ band in the case of the β scenario. It is seen that the minor γ contribution amounts to $\sim$10% of the total at this temperature $T = 0.1T_c$ for both $F_{z(10)}$ and $F_{z(11)}$. Thus in order to understand the field dependence of the form factors, the multiband effect is essential, which further becomes clear later. We note in passing that, as mentioned in the Introduction on MgB_2, Cubitt *et al.* [5] discovered the additional contribution of the minor π band to the main σ band contribution at lower H. This general trend here supports their discovery (see Fig. 2 in Ref. [5]). Note that the relative weight of the main β contribution and minor γ contribution depends on temperature, field, and field orientation Ω. Generally as T and H decrease, the minor γ contribution increases because the two order parameters are more competitive there.

C. Phase diagrams in H vs Ω

Since we have determined the gap ratios for each scenario, it is possible to establish the phase diagrams on the H vs Ω plane. For $H \parallel c$ the two orbital-limited $H^i_{c2,c}$ ratio ($i = \beta, \gamma$) with the obvious notations is written as

$$\frac{H^{\beta}_{c2,c}}{H^{\gamma}_{c2,c}} = \frac{\xi^2_{\gamma,c}}{\xi^2_{\beta,c}} = \left(\frac{\Delta_\beta}{\Delta_\gamma}\right)^2 \left(\frac{v_{\gamma,c}}{v_{\beta,c}}\right)^2. \tag{11}$$

It is known [11] that the Fermi velocity ratio $v_{\gamma,c}/v_{\beta,c} = 0.5$. Thus $H^{\beta}_{c2,c}/H^{\gamma}_{c2,c} = 2.5^2 \times 0.5^2 \sim 1.6$ for the β scenario while $H^{\beta}_{c2,c}/H^{\gamma}_{c2,c} = 1.7^{-2} \times 0.5^2 \sim 0.1$ for the γ scenario, those corresponding to Fig. 1(a) and Fig. 1(c) at $\Omega = 90^\circ$, respectively. On the other hand, at $\Omega = 0^\circ$

$$\frac{H^{\gamma}_{c2,ab}}{H^{\beta}_{c2,ab}} = \frac{\Gamma_\gamma H^{\gamma}_{c2,c}}{\Gamma_\beta H^{\beta}_{c2,c}} = 3 \times \frac{H^{\gamma}_{c2,c}}{H^{\beta}_{c2,c}}. \tag{12}$$

This yields $H^{\beta}_{c2,ab}/H^{\gamma}_{c2,ab} = 3/1.6 \sim 1.9$ for the β scenario while $H^{\beta}_{c2,ab}/H^{\gamma}_{c2,ab} = 3/0.1 \sim 30$ for the γ scenario, thus giving rise to the situations depicted in Fig. 1(a) and Fig. 1(c) at $\Omega = 0^\circ$, respectively. Note that the crossing point A of the two orbital-limited H_{c2}'s in Fig. 1(a) is located at around $\Omega_A \sim 1^\circ$.

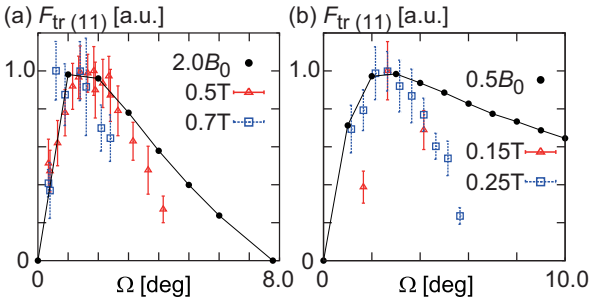

FIG. 7. (Color online) The transverse form factors $F_{tr(11)}$ of the SANS data (open symbols) [12,28] at $H = 0.7$ T and $H = 0.5$ T are compared with the theoretical results (filled symbols) for $B = 2.0$ (a) and the data at $H = 0.25$ T and 0.15 T with $B = 0.5$ ($T = 0.5T_c$) (b).

IV. FORM FACTORS AND VORTEX LATTICE ANISOTROPY

A. Form factors

The form factors FF are a sensitive and useful probe measured by SANS in order to detect the field distribution in the vortex state. The SANS experiments [12,28] on Sr_2RuO_4 are performed. They find the transverse components of FF as a function of Ω near the *ab* plane. Here we obtain FF by evaluating the field distribution via a self-consistent solution of Eq. (3).

It is seen from Figs. 7(a) and 7(b) that the angle Ω dependencies of the transverse component of FF for two fields $B = 2.0$ (high field) and $B = 0.5$ (low field) exhibit a different characteristic: The high-field data show a simple monotonic decrease after taking a maximum towards $\Omega = \Omega_c$ at which the superconducting-normal state transition takes place. The monotonic transverse FF curve is similar to that of the single-band case shown in previous papers [19,31]. This high-field scan ($B = 2.0$) corresponds to the horizontal scanning path in Fig. 1(b) where only the Γ_β region is sensed. The maximum position $\Omega_{max}^{FF} = 0.9^\circ$ coincides with those of the single-band result [19] with $\Gamma = 60$. The overall features of the experimental data for $H = 0.5$ T and 0.7 T are well reproduced as seen from Fig. 7(a) except for a few data points at higher angles.

On the other hand, for the low-field result ($B = 0.5$) shown in Fig. 7(b), it is seen that the theoretical FF curve coincides with the maximum angle of the experimental data at $H =$ 0.15 T and 0.25 T. However, it deviates from those data after that. The experimental data tend to vanish at around $\Omega_c \sim 6^\circ$, which is far from the known $\Omega_c \sim 30^\circ$ (18°) at $H = 0.15$ (0.25) T, which should be ultimate vanishing angle for FF amplitude. We will discuss this discrepancy shortly. Here we just point out that those low-field data correspond to the low-field scanning paths in Fig. 1(b) where the crossover of the regions $\Gamma_\beta \to \Gamma_\gamma \to \Gamma_\beta$ is sensing with increasing Ω.

We decompose the FF contributions from the major β band and the minor γ band for the transverse components $F_{tr(10)}$ (a) and $F_{tr(11)}$ (b) and the longitudinal components $F_{z(10)}$ (c) and $F_{z(10)}$ (d) as shown in Fig. 8 for the high field and Fig. 9 for the low field. The relative weight of the minor component in this transverse FF is around 10% of the total FF and its peak contribution coincides with the maximum position Ω_{max}

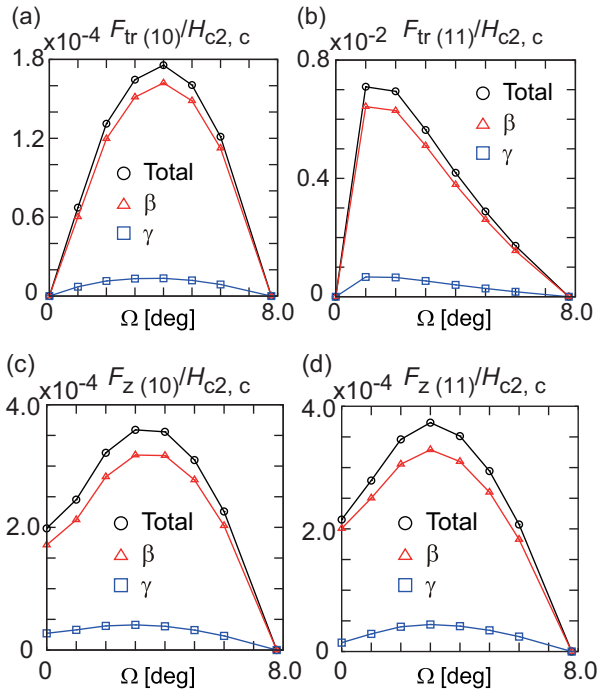

FIG. 8. (Color online) The decomposition of the transverse components of the form factors $F_{tr(10)}$ (a) and $F_{tr(11)}$ (b) at high field $B = 2.0$ ($T = 0.5T_c$). The decomposition of the longitudinal components of the form factors $F_{z(10)}$ (c) and $F_{z(11)}$ (d) at high field $B = 2.0$ ($T = 0.5T_c$).

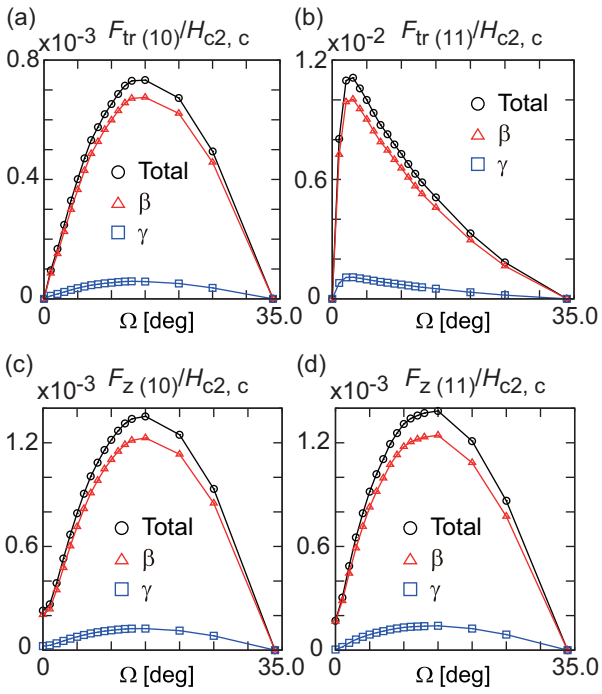

FIG. 9. (Color online) The decomposition of the transverse components of the form factors $F_{tr(10)}$ (a) and $F_{tr(11)}$ (b) at low field $B = 0.5$ ($T = 0.5T_c$). The decomposition of the longitudinal components of the form factors $F_{z(10)}$ (c) and $F_{z(11)}$ (d) at low field $B = 0.5$ ($T = 0.5T_c$).

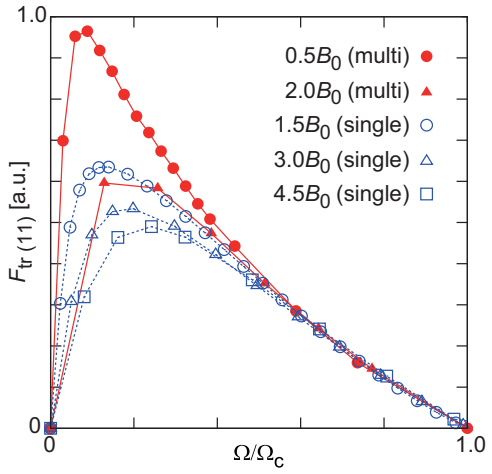

FIG. 10. (Color online) The comparison of the transverse form factors $F_{\mathrm{tr}(11)}$ with the single-band results (open symbols) [19] for $B = 1.5$, 3.0, and 4.5 and the present multiband results (filled symbols) depicted in Fig. 7 for $B = 2.0$ and 0.5. The vertical scale is adjusted so that the slopes of these curves near Ω_c coincide with each other. It is clear that the low-field theoretical result ($B = 0.5$) behaves differently, exhibiting a bimodal structure.

for both $B = 2.0$ (high field) and $B = 0.5$ (low field) data. As for the longitudinal components of $F_{z(10)}$ and $F_{z(10)}$, it is reasonable to see that the maximum angle Ω_{max} is shifted to a higher angle than $F_{\mathrm{tr}(11)}$. This is because when $H_{c2}(\Omega_c)$ is approached the "effective" field virtually increases because the decreasing $\Delta(\Omega)$ means decreasing H_p and hence enhances PPE, thus pushing up the longitudinal FF $|F_z|$.

In order to clearly see the different angle dependencies $F_{\mathrm{tr}(11)}(\Omega)$ for the two cases and to understand the discrepancy of the low-field data mentioned above shown in Fig. 7(b), we replot those theoretical results normalized by Ω_c in Fig. 10 and compare those with the corresponding single-band results [19], where we have adjusted the vertical scale so that the slopes of these curves near Ω_c coincide with each other. It is now seen clearly that

(1) The high-field result $B = 2.0$ belongs to the single-band universality curve. This is because the high-field scanning path is sensing only the Γ_β region in Fig. 1(b). This is virtually the same as in the single-band case—namely, after taking the maximum the FF curve simply goes to vanish at Ω_c.

(2) The low-field result $B = 0.5$ behaves differently from those single-band universality curves and exhibits a "bimodal" Ω dependence where the FF peak is additionally enhanced. Thus the curve just after taking the maximum tends to vanish earlier than at Ω_c which is the ultimate vanishing angle.

Let us come back to understand the low-field FF data shown in Fig. 7(b). The bimodal $F_{\mathrm{tr}(11)}(\Omega)$ structure at the low field is shown in Fig. 9(b) where the slope just after the maximum differs from the slope at higher angles as Ω increases. This crossover angle $\Omega_{\mathrm{cross}} \sim 4^\circ$–$5^\circ$. This low-field scan corresponds to the low-field scanning path in Fig. 1(b), where the crossover of the regions $\Gamma_\beta \rightarrow \Gamma_\gamma \rightarrow \Gamma_\beta$ is sensing with increasing Ω. In particular, the central peak Ω region ($1.0^\circ < \Omega < 4.0^\circ$) in the bimodal structure corresponds to the middle Γ_γ region in this crossover. This theoretical curve is

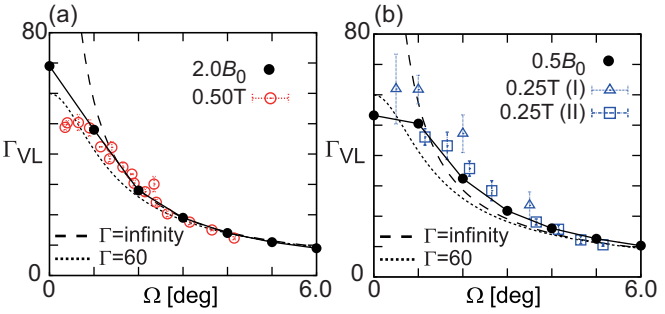

FIG. 11. (Color online) The comparison of the experimental data (open symbols) [12,28] for $\Gamma_{\mathrm{VL}}(\Omega)$ for $H = 0.5$ T with the high-field results of $B = 2.0$ (filled symbols) (a) and $H = 0.25$ T with the low-field results of $B = 0.5$ (filled symbols) (b) ($T = 0.5T_c$). The curves are drawn by the effective mass formula Eq. (10) with $\Gamma = 60$ (dotted line) and $\Gamma = \infty$ (dashed line).

compared with the SANS data [28] at $H = 0.25$ T in Fig. 7(b). Although the present experimental data do not exhibit this bimodal FF structure, the existing data are understood as coming only from the middle Γ_γ region among the bimodal structure because the extrapolated vanishing angle $\Omega_c \sim 7^\circ$. This critical angle is too small compared with $\Omega_c = 18^\circ$ which must be the ultimate vanishing angle of the FF intensity. Thus we interpret this so that the existing FF data are coming for the peak Γ_γ region of the bimodal FF distribution. This interpretation is strengthened later when analyzing the vortex lattice anisotropy Γ_{VL}.

B. Vortex lattice anisotropy Γ_{VL}

Figure 11 shows the results of the vortex lattice anisotropy Γ_{VL} compared with the SANS experiments [28] where for a given B and Ω the self-consistent solutions of Eq. (3) are optimized for varying Γ_{VL} as shown in Fig. 12 to seek the free energy minimum where the free energy form is given by Eq. (1). In general the optimized Γ_{VL} is that given neither

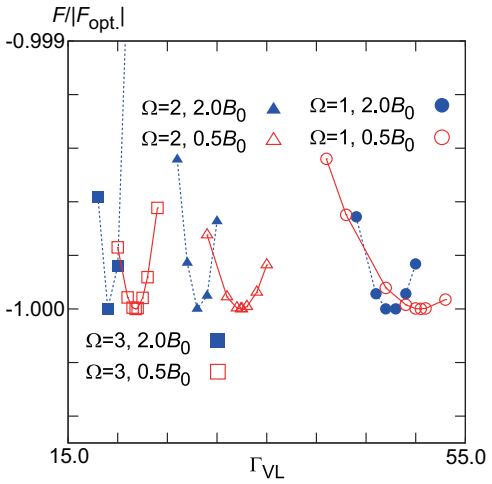

FIG. 12. (Color online) The free energy curves for various angles Ω as a function of Γ_{VL} for $B = 2.0$ (filled symbols) and $B = 0.5$ (open symbols) in order to emphasize that our computations are performed accurately enough to resolve the subtle differences of the Γ_{VL} values.

by the effective mass anisotropies $\Gamma_\beta(\Omega)$ with $\Gamma_\beta = 60$ nor $\Gamma_\gamma(\Omega)$ with $\Gamma_\gamma = 180$ alone given by Eq. (10). This is obvious because those two anisotropies are coupled and competed by the multiband effect.

The higher field results in Fig. 11 (a) follow rather well those given by the above formula of Eq. (10) for $\Gamma_\beta(\Omega)$ for the higher angles $\Omega > 3^\circ$. We note that at $\Omega = 0^\circ$, $\Gamma_{\rm VL}(0^\circ) = 70$ corresponds precisely to the anisotropy $H^\beta_{c2}(0^\circ)/H^\beta_{c2}(90^\circ)$ for $T = 0.5T_c$. Between the angle $1^\circ < \Omega < 3^\circ$, the theoretical results deviate upwards; that is, $\Gamma_{\rm VL}(\Omega) > \Gamma_\beta(\Omega)$. The high-field scan in Fig. 1(b) is barely touching the Γ_γ region whose anisotropy can be certainly larger than $\Gamma_\beta = 60$ because $\Gamma_\gamma = 180$.

The low-field theoretical results shown in Fig. 11(b) follow the $\Gamma_\beta(\Omega)$ curve for $0^\circ \leqslant \Omega < 1^\circ$ and remarkably exceed the $\Gamma \to \infty$ curve in $1^\circ < \Omega < 5^\circ$. This window in Ω corresponding to the Γ_γ region appears because there the $\Gamma_\gamma = 180$ anisotropy further modifies the $\Gamma_{\rm VL}$ value upwards, simultaneously enhancing the transverse FF. We point out a theoretical fact that as $\Gamma_{\rm VL}(\Omega)$ increases, $F_{\rm tr}(\Omega)$ becomes larger. We anticipate that the results at lower temperatures than the present one at $T = 0.5T_c$ would improve the quantitative fittings of $\Gamma_{\rm VL}$ and simultaneously $F_{\rm tr}(\Omega)$. Note that $\Gamma_{\rm VL}(\Omega = 0^\circ) = 52$ corresponds to the single-band anisotropy for the β band at lower fields [19]. The $H = 0.25$ T data nicely fit our theoretical result. The important point here is that not only the experimental data exceed the $\Gamma \to \infty$ line, but also there exists a wider window $1^\circ < \Omega < 5^\circ$ where the experimental data deviate from the single-band $\Gamma_\beta(\Omega)$ curve.

We demonstrate in Fig. 12 that the optimal $\Gamma_{\rm VL}$ is determined careful enough, which can be larger than the corresponding $\Gamma \to \infty$ case in Eq. (10). For example, for our $B = 0.5$ case at $\Omega = 2^\circ$ our $\Gamma_{\rm VL} = 32$ while $\Gamma_{\rm VL} = 29$ for $\Gamma = \infty$ and $\Gamma_{\rm VL} = 28$ for $\Gamma_\beta = 60$. Thus it can be said that the multiband effect helps enhancing $\Gamma_{\rm VL}$ beyond $\Gamma = \infty$.

C. Order parameters, free energy, and magnetization

We illustrate the Ω dependencies of several physical quantities of interest which are the basis of the form factors and magnetic torque calculations as shown shortly. The free energy $F(\Omega)$ is shown in Fig. 13, from which we will evaluate the magnetic torques. Since the transition at Ω_c is of second order at those fields and temperature ($T = 0.5T_c$), $F(\Omega)$ becomes zero smoothly at the transition point Ω_c .

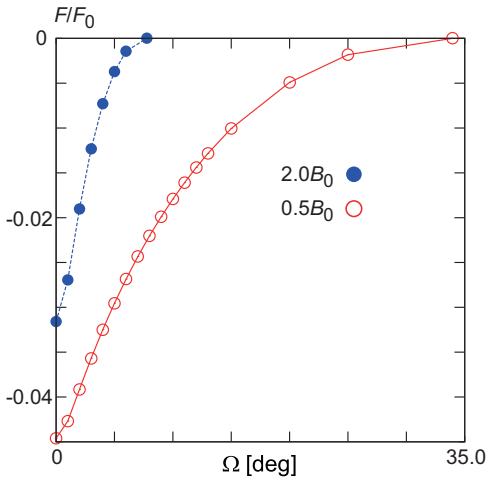

FIG. 13. (Color online) The angle dependencies of the free energy for $B = 2.0$ (filled symbols) and $B = 0.5$ (open symbols), showing a smooth change of the second-order transition at Ω_c, where $\Omega_c = 7.78^\circ$ and $\Omega_c = 33.96^\circ$, respectively.

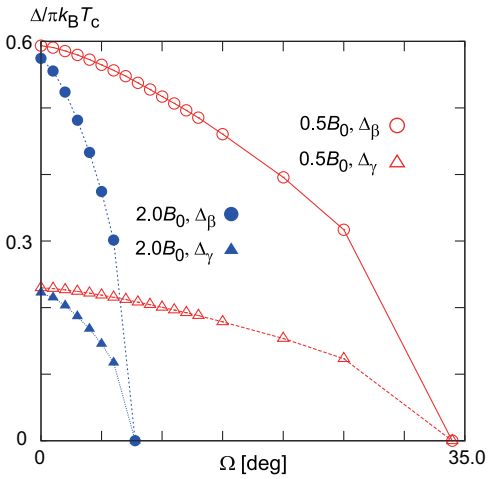

FIG. 14. (Color online) The angle dependencies of the order parameter amplitudes $\Delta_\beta(\Omega)$ and $\Delta_\gamma(\Omega)$ at the center of the vortex unit cell for $B = 2.0$ (filled symbols) and $B = 0.5$ (open symbols).

As seen from Fig. 14, the two order parameters—the major $\Delta_\beta(\Omega)$ and minor $\Delta_\gamma(\Omega)$—start decreasing from $\Omega = 0^\circ$ towards Ω_c as a function of Ω. The two curves change smoothly in parallel because the minor component $\Delta_\gamma(\Omega)$ is induced by the major one $\Delta_\beta(\Omega)$ through the Cooper pair transfer V_{12} in the absence of V_{22}. In this case we expect no hidden first-order transition phenomena [10], where there is an abrupt change of the two order parameters inside the superconducting state.

In Fig. 15 the total paramagnetic susceptibility $\chi_t(\Omega)$ and decomposed $\chi_\beta(\Omega)$ and $\chi_\gamma(\Omega)$ are displayed as a function of Ω. Since we assume the density of states $N_{F\gamma} = 43\%$ and $N_{F\beta} = 57\%$ of the total DOS, the corresponding paramagnetic values $\chi_\gamma(\Omega) > \chi_\beta(\Omega)$ as expected. We also point out that the base paramagnetic moment value at $\Omega = 0^\circ$ is large because

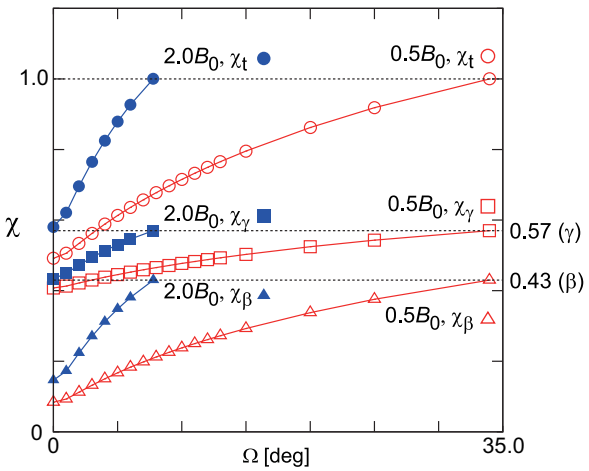

FIG. 15. (Color online) The angle dependencies of the paramagnetic susceptibility $\chi_t(\Omega)$ for $B = 2.0$ (filled symbols) and $B = 0.5$ (open symbols), which are decomposed into $\chi_\beta(\Omega)$ and $\chi_\gamma(\Omega)$.

the calculations are done at rather high temperature $T = 0.5T_c$. Needless to say, at $T \to 0$, χ_t should vanish at $\Omega = 0^\circ$. As Ω increases $\chi_t(\Omega)$ becomes larger because the system is approaching the transition point at Ω_c where the normal value χ_N must be recovered; that is, $\chi_t(\Omega_c) = \chi_N$.

V. MAGNETIC TORQUES

Magnetic torque $\tau(\Omega)$ defined by $\tau(\Omega) = \partial F(\Omega)/\partial\Omega$ provides several important pieces of information on a uniaxial anisotropic superconductor. We can know the intrinsic anisotropy of a system by the peak position of the torque curve $\tau(\Omega)$. This can be easily performed by using a phenomenological theory based on London theory [41] for single-band superconductors. In our previous papers [19,31] we examine the applicability of this approach and propose a modification to this. Extending these single-band Eilenberger calculations, here we show the results of the torque curves $\tau(\Omega)$ for the present two-band model and use those to analyze the data on Sr_2RuO_4, where the torque curves have been measured recently [29].

We first display our results for the torque curves in Fig. 16 where our results for $B = 2.0$ and $B = 0.5$ are compared with the experimental data for $H = 0.5$ T (former) and $H = 0.2$ T (latter). It is seen from Fig. 16(a) at the high field $B = 2.0$ that the fitting is done well, such as the peak position and the Ω_c value. Since the high-field result is sensing only on the Γ_β region, it is reasonable that the theoretical curve nicely explains the experimental data at $H = 0.5$ T and the peak position $\Omega_{peak}^{torque} = 1.5^\circ$ coincides with the single-band result [19]. This peak position Ω_{peak}^{torque} also coincides with Ω_{peak}^{FF} of the form factor ($B = 2.0$). Thus the four values Ω_{peak}^{torque} and Ω_{peak}^{FF} both for theory and experiment are coinciding with each other, leading us to firmly conclude that in high fields the system is virtually in the single-band-like Γ_β region.

On the other hand, the low-field result ($B = 0.5$) shown in Fig. 16(b) explains the experimental torque curves for $H = 0.2$ T, but the peak positions differ slightly from each other. We also notice here that the theoretical $\Omega_{peak}^{torque} \neq \Omega_{peak}^{FF}$ and Ω_{peak}^{FF} ($\sim 4^\circ$) agrees with the experimental data as shown before.

It is interesting to compare our torque curves with those for the single-band case, which are displayed in Fig. 17. It is seen that the two torque curves nicely correspond to the single-band curves, which is in contrast with the FF case shown in Fig. 10,

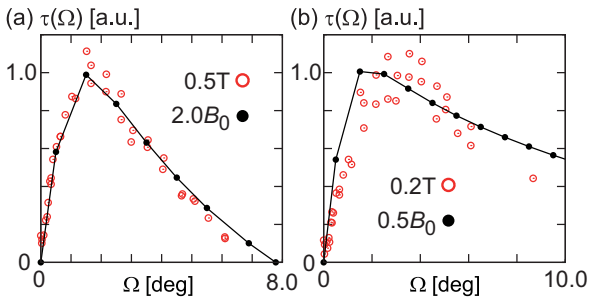

FIG. 16. (Color online) The angle dependencies of the torques (filled symbols) for $B = 2.0$ together with the experimental data (open symbols) [29] of $H = 0.5$ T (a) and $B = 0.5$ with the data of $H = 0.2$ T (b).

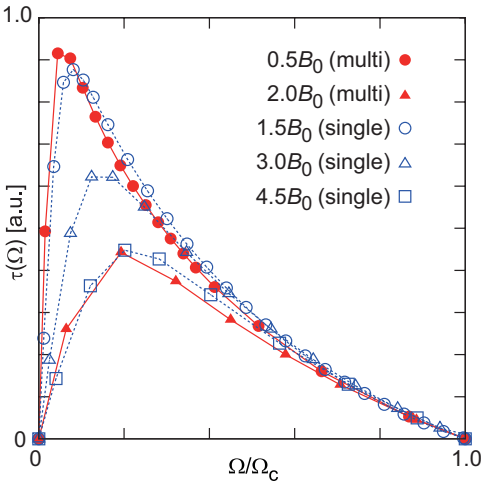

FIG. 17. (Color online) The torque curves as a function of Ω for $B = 2.0$ and $B = 0.5$ at $T = 0.5T_c$. These are compared with the single-band results [19] for $B = 1.5$, 3.0, and 4.5. The vertical scale is adjusted so that the slopes of these curves near Ω_c coincide with each other.

where the low-field curve markedly deviates from the single-band case. This means that the magnetic torque is a rather insensitive probe to see the subtle but important multiband effect. In other words, the form factor measurement is sensitive enough to distinguish the multiband effect from the single-band effect. This is because the torque $\tau(\Omega) = \partial F(\Omega)/\partial\Omega$ comes from the total free energy $F(\Omega)$ while the FF is probing the particular Fourier component of the spatially modulated magnetic field in the mixed state selectively. Thus it is natural to expect that the FF measurement is more sensitive than the torque measurement in picking up the multiband effect.

VI. DISCUSSION

A. Single band vs multiband

In order to describe the transverse components of FF and Γ_{VL} data [28] near the ab plane, which is the main theme of the paper, we have done the calculations based on both scenarios, first focusing on the $H \parallel c$ physics to fix the model parameters. Here we critically examine those scenarios comparatively. It is obvious that the multiband scenario is superior to the single-band scenario [19] because the former includes the latter as a limiting case. A question is how effectively the single-band scenario can describe those data or how the multiband description is inevitable for the Sr_2RuO_4 physics. As already demonstrated and also shown in Fig. 18, the overall features of those data can be reproduced by the single-band model with $\Gamma_\beta = 60$ in the higher fields above $H > 0.5$ T in the H vs Ω plane, where there is a little trace of the existence of the γ band with $\Gamma_\gamma = 180$ [see Fig. 18(a)]. In this sense the single-band picture is enough for this region. In contrast, however, it is necessary to retain the γ band contribution in addition to the major β band contribution in the low-field region below 0.5 T [see Fig. 18(b)]. The former contribution is hidden and not explicit where the crossover occurs around $\Omega = 1.5^\circ$ as indicated in Fig. 18(b). This is necessary and indispensable to take it into account

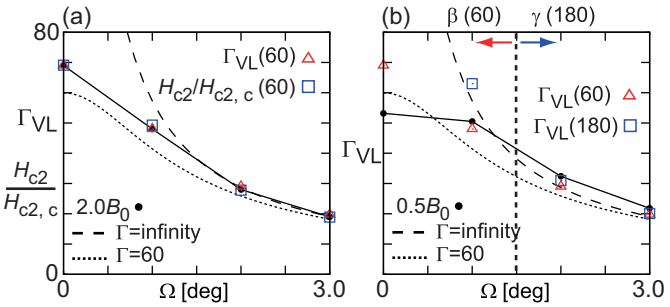

FIG. 18. (Color online) The comparison of the Γ_{VL} with the single-band cases $\Gamma_{VL}(60)$ and $\Gamma_{VL}(180)$ and also with the H_{c2} anisotropy $H_{c2}(\Omega)/H_{c2,c}$. (a) High-field case 2.0 where the three data Γ_{VL}, $\Gamma_{VL}(60)$, and $H_{c2}/H_{c2,c}$ coincide with each other, and (b) low-field case 0.5 where the lower (high) angle region corresponds to the β (γ) band anisotropy. The vertical dashed line at around $\Omega = 1.5^\circ$ denotes its boundary. The dotted (dashed) curves indicate the angle dependence of the effective mass formula Eq. (10) for $\Gamma = 60$ ($\Gamma = \infty$).

for explaining the FF and Γ_{VL} data [28]. This is a part of the reasons why our single-band theory [19] is successful to understand the mixed state properties of the present strongly uniaxial anisotropic superconductor. Moreover, depending on the physical quantities of interest, the multiband effect is not so apparent even in the low-field region. Namely, the torque curves are quite insensitive to the presence of the minor band and all the theoretical torque curves collapse into a universal curve by appropriate scaling as discussed before (see Fig. 17).

B. β main scenario vs γ main scenario

The question on which band the gap is large is much discussed in connection with the pairing mechanism to stabilize the chiral p-wave state by many authors [13–17]. Here we take a different view to consider this question through the analysis of the FF, Γ_{VL}, and torques. If the γ band is major, this survives in the high field region of the H vs Ω plane over the minor β band (see Figs. 1(c) and 1(d)). Then the SANS experiment should detect it, manifesting itself in Γ_{VL}; that is, $\Gamma_{VL} \to 180$ as $\Omega \to 0$. However, both high-field and low-field data shown in Fig. 11 indicate $\Gamma_{VL} \sim 60$ or so, which is direct evidence that the β band with $\Gamma_\beta = 60$ is major. This conclusion is also supported by the H_{c2} ratio $H_{c2,ab}(T)/H_{c2,c}(T) \to 60$ when $T \to T_c$ [39] because near T_c this ratio directly reflects the intrinsic Fermi velocity anisotropy [42], or the coherent length anisotropy. Thus those experimental data obviously reveal that the β band is major with certainty.

C. Cooper pair tunneling V_{12} vs direct attraction V_{22} : Hidden first order

In general, for the two-band scenario containing the three pairing parameters, V_{11} (V_{22}) is the attractive interaction for the major (minor) band, and $V_{12} = V_{21}$ is the Cooper pair tunneling term or proximity-induced term. Here we set $V_{22} = 0$ in this paper because there is no or little indication for $V_{22} \neq 0$, which causes the so-called hidden first order phenomena [10]. Namely at H^* inside H_{c2} certain physical quantities exhibit a sudden change as a function of H, such as the Sommerfeld coefficient $\gamma(H)$ or the magnetization curve as observed in $CeCu_2Si_2$ [6], UBe_{13} [7], and KFe_2As_2 [8]. This means that $V_{22} \sim 0$ in Sr_2RuO_4 and the minor γ band pairing is exclusively induced by the major γ band through V_{12}.

D. Expected low-T behaviors

Because of several technical reasons our main computations have been done at relatively high T, namely $T = 0.5T_c$, which are nevertheless successful in capturing the characteristic features in the FF, Γ_{VL}, and torques in a qualitative level. To understand those data in a quantitative level it is necessary to go into lower T which is demanding computationally. Here we anticipate possible outcomes if performing it. As shown in Fig. 7 we have mentioned that the low-field FF ($B = 0.5$) differs from that in $B = 2.0$, which belongs to the single-band universality class. The FF in low angle Ω is enormously enhanced by the assistance from the minor band which amounts almost 10% even at $T = 0.5T_c$. In low-T calculation this enhancement of the FF should increase and the FF angle dependence becomes more similar to the data shown in Fig. 7(b). This expectation is reasonable because at lower T the induced paramagnetic moments are confined in the vortex core, making more contrast in the spatial field distribution and thus enhancing the FF amplitude. See also Fig. 15 where the paramagnetic susceptibility or paramagnetic moments of the minor γ band are almost exhausted at $\Omega = 0$ to its normal value, meaning that is not confined in the core. Thus, the paramagnetic moments are spreading out the whole space uniformly.

E. Other multiband superconductors with PPE

We can deepen our understandings of the present material by comparing similar multiband superconductors, $CeCu_2Si_2$ [6], UBe_{13} [7], and KFe_2As_2 [8]. The first two are heavy-fermion materials known to have multiband with all full gaps belonging to the spin singlet category, where H_{c2} is strongly suppressed and the hidden first order like anomalies at H^* exist. Thus as mentioned V_{22} is indispensable for those systems. According to the recent SANS experiment [9] the typical multiband Fe pnictide KFe_2As_2 is similar to Sr_2RuO_4 in the point that the vortex anisotropy Γ_{VL} observed differs from the H_{c2} anisotropy. This can be also explained by PPE. Thus the present theoretical framework, which is quite general, might be able to explain those systems.

F. Gap structure: Vertical line node vs horizontal line node

We have assigned the nodal structure that the dominant β band is a full gap while the minor γ is vertical line nodes, in order to reproduce the square vortex lattice oriented to the (110) direction observed for $H \parallel c$ which dominates the whole space measured in the H vs T phase [40]. The gap (or near) nodes should be in this direction in reciprocal space [43], implying a $d_{x^2-y^2}$-like nodal structure, contrary to the claim by Deguchi *et al.* [37], who measure the specific heat by rotating the field direction and see the fourfold oscillation patterns whose minima are located for the (100) direction. They conclude that the γ band has a d_{xy}-like nodal structure. However, this assignment is difficult for explaining the square

vortex lattice orientated along the (110) direction for $H \parallel c$, even if we take into account the in-plane Fermi velocity anisotropy in the β and α bands whose minima are oriented along the (100) direction [44], thus preferring the square lattice oriented along the (100) direction as discussed previously [45]. Thus the best way to avoid this difficulty is to simply consider that the γ band nodal structure is $d_{x^2-y^2}$-like. The specific heat oscillation experiment done above 120 mK is still too high to see the sign changing of the oscillation pattern because the γ band is minor where the expected sign-changing temperature theoretically [35] and experimentally [46] usually located at $0.1T_c \sim 150$ mK must be lowered.

This kind of the band-dependent nodal structure differs from the idea based on the symmetry-protected nodal structure where all plural bands are governed by the same gap symmetry. From this point of view, it is possible that the $d_{x^2-y^2}$ nodal structure may not be truly sign-changing symmetry, but rather an extended s-wave type with the anisotropic gap whose minima are along the (110) direction.

Some authors [47] assert that the horizontal line nodes are compatible with a chiral triplet state $(p_x + ip_y)\cos p_z$. From the present point of view, the Sommerfeld coefficient $\gamma(H)$ behavior for $H \parallel c$ may not be consistent with this, which gives a too larger $\gamma(H)$ at low-field region than the experimental data [37] shown in Fig. 4. In this connection we should mention that no one succeeded in explaining the $\gamma(H)$ behavior [37] for $H \parallel ab$. In particular, it is viewed that the initial rise of $H \parallel ab$ is often assigned to the $\alpha + \beta$ DOS because the plateau of $\gamma(H)$ for this midfield region $H \sim 0.4$–0.5 T seems to correspond to $\alpha + \beta$ DOS (43% of the total), which was taken as supporting evidence of the γ major scenario. Since we cannot accept this view anymore, a full understudying of the $\gamma(H)$ behavior for $H \parallel ab$ remains a mystery.

G. Perspectives—Future experiments: Knight shift and FFLO

There remain certainly important experiments to further the research front of this interesting material: NMR experiments have been extensively done [11], showing the absence of any change of the Knight shift [48] below T_c. This is interpreted as a freely rotatable d-vector in a spin triplet pairing, keeping it always perpendicular to an external field which is as small as ~mT, a big mystery because according to the recent ARPES [49] and RIXS [50] the spin-orbit coupling which locks the d-vector to the crystalline lattice is on the order of 200 mV. The recent magnetization experiment [29] is directly able to detect the spin susceptibility change at the first-order transition $H_{c2,ab}$, which amounts to a ~10% drop compared with the normal value. This is in sharp contrast with the Knight shift experiment by NMR which calls for reexamination of NMR experiments.

Here we propose the T_1 measurement to detect the FFLO state [51,52] expected to exist along $H_{c2,ab}$ below $T \simeq 0.8$ K, where the first-order transition is observed. Recently anomalous T_1^{-1} enhancement is observed [53] when entering the FFLO state due to the appearance of the zero-energy state at the domain walls where the FFLO order parameter is π-shifted. There is a good chance to observe it if the second phase below $H_{c2,ab}$ really exists, which we believe so. A necessary condition is that T_2 is short enough so that the spin-lattice relaxation T_1 process is dominated through those zero energy states as in the κ-(BEDT-TTF)$_2$Cu(NCS)$_2$ case [53]. In this connection we mention a recent μSR experiment [54] that probes the peculiar vortex morphology at low fields of $H \parallel c$ and related theory based on hidden criticality associated with multibandness [55–57].

VII. SUMMARY AND CONCLUSION

Based on the microscopic Eilenberger theory extended to a multiband case, we have studied the mixed state properties of a uniaxial anisotropic type II superconductor, focusing on the interplay between the Pauli paramagnetic effect and multiband effect. A two-band model calculation is set up and applied to Sr_2RuO_4. We have succeeded in reproducing the data of both the form factors of SANS experiments [12,28] and magnetic torque experiment [29]. That leads us to the conclusion that to understand the physics in Sr_2RuO_4 it is indispensable to consider both the Pauli paramagnetic effect and multiband effect simultaneously, which conspire to give rise to a variety of mysteries associated with the pairing symmetry determination in this material.

As agreed with the previous identification based on the single-band analysis [19], the pairing symmetry in Sr_2RuO_4 is either singlet, which is most likely, or triplet with the d-vector locked in the ab plane, which is less likely. The β (γ) band is major (minor) with the mass anisotropy 60 (180). Namely, the β (γ) band has a larger (smaller) gap. The gap structure is a full gap in the β band while in the γ band it is $d_{x^2-y^2}$-like. This simple picture was difficult to reach because of the extreme two-dimensionality of this material, which prevents conventional experimental access. Now the dedicated and refined experimental tools [12,29,58,59] which are able to align the magnetic field direction accurately to within 1° enable us to uncover the physics of Sr_2RuO_4.

ACKNOWLEDGMENTS

The authors thank M. R. Eskildsen, S. Kuhn, and C. Rastovski for providing us unpublished SANS data and also M. Ichioka, M. Ishihara, and Y. Amano for discussions on the theoretical side, and S. Kittaka, A. Kasahara, T. Sakakibara, K. Ishida, Y. Maeno, S. Yonezawa, and M. Takigawa for discussions on the experiment side. K.M. is supported by Grants-in-Aid for Scientific Research No. 26400360 and No. 25103716 from the Japan Society for the Promotion of Science.

[1] M. V. Milošević and A. Perali, Supercond. Sci. Technol. **28**, 060201 (2015).
[2] J. Nagamatsu, N. Nakagawa, T. Muranaka, Y. Zenitani, and J. Akimitsu, Nature (London) **410**, 63 (2001).
[3] J. Kortus, I. I. Mazin, K. D. Belashchenko, V. P. Antropov, and L. L. Boyer, Phys. Rev. Lett. **86**, 4656 (2001).
[4] T. Hirano, K. Takamori, M. Ichioka, and K. Machida, J. Phys. Soc. Jpn. **82**, 063708 (2013).

[5] R. Cubitt, M. R. Eskildsen, C. D. Dewhurst, J. Jun, S. M. Kazakov, and J. Karpinski, Phys. Rev. Lett. **91**, 047002 (2003).
[6] S. Kittaka, Y. Aoki, Y. Shimura, T. Sakakibara, S. Seiro, C. Geibel, F. Steglich, H. Ikeda, and K. Machida, Phys. Rev. Lett. **112**, 067002 (2014).
[7] Y. Shimizu, S. Kittaka, T. Sakakibara, Y. Haga, E. Yamamoto, H. Amitsuka, Y. Tsutsumi, and K. Machida, Phys. Rev. Lett. **114**, 147002 (2015).
[8] S. Kittaka, Y. Aoki, N. Kase, T. Sakakibara, T. Saito, H. Fukazawa, Y. Kohori, K. Kihou, Chul-Ho Lee, A. Iyo, H. Eisaki, K. Deguchi, N. K. Sato, Y. Tsutsumi, and K. Machida, J. Phys. Soc. Jpn. **83**, 013704 (2014).
[9] S. Kuhn and M. R. Eskildsen (private communication).
[10] Y. Tsutsumi, K. Machida, and M. Ichioka, Phys. Rev. B **92**, 020502(R) (2015).
[11] A. P. Mackenzie and Y. Maeno, Rev. Mod. Phys. **75**, 657 (2003).
[12] C. Rastovski, C. D. Dewhurst, W. J. Gannon, D. C. Peets, H. Takatsu, Y. Maeno, M. Ichioka, K. Machida, and M. R. Eskildsen, Phys. Rev. Lett. **111**, 087003 (2013).
[13] M. E. Zhitomirsky and T. M. Rice, Phys. Rev. Lett. **87**, 057001 (2001).
[14] T. Nomura and K. Yamada, J. Phys. Soc. Jpn. **69**, 3678 (2000); **71**, 404 (2002); **71**, 1993 (2002).
[15] S. Raghu, A. Kapitulnik, and S. A. Kivelson, Phys. Rev. Lett. **105**, 136401 (2010).
[16] Q. H. Wang, C. Platt, Y. Yang, C. Honerkamp, F. C. Zhang, W. Hanke, T. M. Rice, and R. Thomale, Europhys. Lett. **104**, 17013 (2013).
[17] T. Scaffidi, J. C. Romers, and S. H. Simon, Phys. Rev. B **89**, 220510(R) (2014).
[18] K. Machida and M. Ichioka, Phys. Rev. B **77**, 184515 (2008).
[19] Y. Amano, M. Ishihara, M. Ichioka, N. Nakai, and K. Machida, Phys. Rev. B **91**, 144513 (2015).
[20] G. Eilenberger, Z. Phys. **214**, 195 (1968).
[21] A. I. Larkin and Yu. N. Ovchinnikov, in *Nonequilibrium Superconductivity*, edited by D. N. Langenberg and A. I. Larkin (Elsevier, Amsterdam, 1984).
[22] K. Usadel, Phys. Rev. Lett. **25**, 507 (1970).
[23] A. E. Koshelev and A. A. Golubov, Phys. Rev. Lett. **90**, 177002 (2003).
[24] M. Ichioka, K. Machida, N. Nakai, and P. Miranović, Phys. Rev. B **70**, 144508 (2004).
[25] A. B. Vorontsov, M. G. Vavilov, and A. V. Chubukov, Phys. Rev. B **81**, 174538 (2010).
[26] R. M. Fernandes and J. Schmalian, Phys. Rev. B **82**, 014521 (2010).
[27] A. Moor, A. F. Volkov, and K. B. Efetov, Phys. Rev. B **83**, 134524 (2011).
[28] M. R. Eskidsen (private communication).
[29] S. Kittaka, A. Kasahara, T. Sakakibara, D. Shibata, S. Yonezawa, Y. Maeno, K. Tenya, and K. Machida, Phys. Rev. B **90**, 220502(R) (2014).
[30] M. Ishihara, Y. Amano, M. Ichioka, and K. Machida, Phys. Rev. B **87**, 224509 (2013).
[31] Y. Amano, M. Ishihara, M. Ichioka, N. Nakai, and K. Machida, Phys. Rev. B **90**, 144514 (2014).
[32] M. Ichioka, A. Hasegawa, and K. Machida, Phys. Rev. B **59**, 8902 (1999); **59**, 184 (1999).
[33] M. Ichioka and K. Machida, Phys. Rev. B **76**, 064502 (2007); M. Ichioka, K. M. Suzuki, Y. Tsutsumi, and K. Machida, in *Superconductivity: Theory and Applications*, edited by A. M. Luiz (InTech, Croatia, 2011), Chap. 10.
[34] M. M. Doria, J. E. Gubernatis, and D. Rainer, Phys. Rev. B **41**, 6335 (1990).
[35] M. Hiragi, K. M. Suzuki, M. Ichioka, and K. Machida, J. Phys. Soc. Jpn. **79**, 094709 (2010).
[36] P. G. Kealey, D. Charalambous, E. M. Forgan, S. L. Lee, S. T. Johnson, P. Schleger, R. Cubitt, D. McK. Paul, C. M. Aegerter, S. Tajima, and A. Rykov, Phys. Rev. B **64**, 174501 (2001).
[37] K. Deguchi, Z. Q. Mao, and Y. Maeno, J. Phys. Soc. Jpn. **73**, 1313 (2004).
[38] H. Padamsee, J. E. Neighbor, and C. A. Shiffman, J. Low Temp. Phys. **12**, 387 (1973); F. Bouquet, Y. Wang, and R. A. Fisher, Europhys. Lett. **56**, 856 (2001).
[39] S. Kittaka, T. Nakamura, Y. Aono, S. Yonezawa, K. Ishida, and Y. Maeno, Phys. Rev. B **80**, 174514 (2009); J. Phys.: Conf. Ser. **150**, 052112 (2009).
[40] P. G. Kealey, T. M. Riseman, E. M. Forgan, L. M. Galvin, A. P. Mackenzie, S. L. Lee, D. McK. Paul, R. Cubitt, D. F. Agterberg, R. Heeb, Z. Q. Mao, and Y. Maeno, Phys. Rev. Lett. **84**, 6094 (2000).
[41] V. G. Kogan, Phys. Rev. Lett. **89**, 237005 (2002).
[42] P. Miranović, K. Machida, and V. Kogan, J. Phys. Soc. Jpn. **72**, 221 (2003).
[43] N. Nakai, P. Miranović, M. Ichioka, and K. Machida, Phys. Rev. Lett. **89**, 237004 (2002).
[44] D. J. Singh, Phys. Rev. B **52**, 1358 (1995).
[45] R. Heeb and D. F. Agterberg, Phys. Rev. B **59**, 7076 (1999).
[46] K. An, T. Sakakibara, R. Settai, Y. Onuki, M. Hiragi, M. Ichioka, and K. Machida, Phys. Rev. Lett. **104**, 037002 (2010).
[47] Y. Hasegawa, K. Machida, and M. Ozaki, J. Phys. Soc. Jpn. **69**, 336 (2000).
[48] G. M. Androes and V. D. Knight, Phys. Rev. **121**, 779 (1961).
[49] C. N. Veenstra, Z.-H. Zhu, M. Raichle, B. M. Ludbrook, A. Nicolaou, B. Slomski, G. Landolt, S. Kittaka, Y. Maeno, J. H. Dil, I. S. Elfimov, M. W. Haverkort, and A. Damascelli, Phys. Rev. Lett. **112**, 127002 (2014).
[50] C. G. Fatuzzo, M. Dantz, S. Fatale, P. Olalde-Velasco, N. E. Shaik, B. Dalla Piazza, S. Toth, J. Pelliciari, R. Fittipaldi, A. Vecchione, N. Kikugawa, J. S. Brooks, H. M. Rønnow, M. Grioni, Ch. Rüegg, T. Schmitt, and J. Chang, Phys. Rev. B **91**, 155104 (2015).
[51] P. Fulde and R. A. Ferrell, Phys. Rev. **135**, A550 (1964).
[52] A. I. Larkin and Y. N. Ovchinnikov, Zh. Eksp. Teor. Fiz. **47**, 1136 (1964) [Sov. Phys. JETP **20**, 762 (1965)].
[53] H. Mayaffre, S. Krämer, M. Horvatić, C. Berthier, K. Miyagawa, K. Kanoda, and V. F. Mitrović, Nat. Phys. **10**, 928 (2014).
[54] S. J. Ray, A. S. Gibbs, S. J. Bending, P. J. Curran, E. Babaev, C. Baines, A. P. Mackenzie, and S. L. Lee, Phys. Rev. B **89**, 094504 (2014).
[55] L. Komendová, Yajiang Chen, A. A. Shanenko, M. V. Milošević, and F. M. Peeters, Phys. Rev. Lett. **108**, 207002 (2012).
[56] M. Silaev and E. Babaev, Phys. Rev. B **84**, 094515 (2011).
[57] M. Silaev and E. Babaev, Phys. Rev. B **85**, 134514 (2012).
[58] S. Yonezawa, T. Kajikawa, and Y. Maeno, Phys. Rev. Lett. **110**, 077003 (2013).
[59] S. Yonezawa, T. Kajikawa, and Y. Maeno, J. Phys. Soc. Jpn. **83**, 083706 (2014).